Title:	A hybrid permanent magnet and wound field synchronous machine with displaced reluctance axis capable of symmetric four quadrant operation
Authors:	Patrick Winzer, Martin Doppelbauer
Institute:	Karlsruhe Institute of Technology (KIT) Elektrotechnisches Institut (ETI) Hybrid Electric Vehicles (HEV)
Type:	Conference Proceedings
Published at:	2016 18th European Conference on Power Electronics and Applications (EPE'16 ECCE Europe), Karlsruhe, 2016 Publisher: IEEE, Piscataway (NJ) Year: 2016 ISBN: 978-9-0758-1524-5 Pages: 1-11
Hyperlinks:	DOI: https://doi.org/10.1109/EPE.2016.7695296

A Hybrid Permanent Magnet and Wound Field Synchronous Machine with Displaced Reluctance Axis Capable of Symmetric Four Quadrant Operation

Patrick Winzer and Martin Doppelbauer
Karlsruhe Institute of Technology (KIT)
Elektrotechnisches Institut (ETI) – Hybrid Electric Vehicles (HEV)
Kaiserstr. 12, 76131 Karlsruhe, Germany
Phone: +49 (0) 721 608-41955
Fax: +49 (0) 721 608-42921
Email: patrick.winzer@kit.edu
URL: http://www.eti.kit.edu

Keywords

≪AC machine≫, ≪Adjustable speed drive≫, ≪Efficiency≫, ≪Electrical machine≫, ≪Synchronous motor≫, ≪Test bench≫, ≪Variable speed drive≫

Abstract

This paper presents a novel hybrid permanent magnet and wound field synchronous machine geometry with a displaced reluctance axis. This concept is known for improving motor operation performance and efficiency at the cost of an inferior generator operation. To overcome this disadvantage, the proposed machine geometry is capable of inverting the magnetic asymmetry dynamically. Thereby, the positive effects of the magnetic asymmetry can be used in any operation point. This paper examines the theoretical background and shows the benefits of this geometry by means of simulation and measurement. The prototype achieves an increase in torque of 4 % and an increase in efficiency of 2 percentage points over a conventional electrically excited synchronous machine.

Introduction

Since the development of inverter fed drives, a lot of research has been done to optimize the performance of the drive system. The ideal motor drive according to [1] has two main characteristics: First, it has unity inverter utilization, which means that it offers maximum torque in the base speed range, and constant power in the field weakening range, while not being limited to a maximum speed. Second, it has no losses in all operation points. Both characteristics are impossible to achieve fully in real-world systems. However, depending on the machine type, they can be approximated to a certain degree.

While induction and reluctance machines have good field weakening characteristics, they offer rather low torque due to the required magnetizing current [2]. Permanent magnet synchronous machines (PMSM) have very good peak efficiency, however, they show rather inferior field weakening performance when they are designed for maximum torque [1]. Conventional electrically excited synchronous machines (EESM) can be designed to exhibit high torque as well as near-ideal field weakening characteristics [3], yet they suffer from additional losses caused by the rotor excitation current which deteriorates efficiency.

As an interesting compromise, hybrid excited synchronous machines (HSM) have been investigated, which combine permanent magnet (PM) and electric excitation [4]. While maintaining the performance of conventional EESM, efficiency can be increased as the required field exciting current is lower due to the pre-magnetization by means of the PMs.

A further step of development has been investigated in [5], where the effect of a displaced reluctance axis in order to maximize torque has been utilized. This analysis suggested a hybrid excitation synchronous
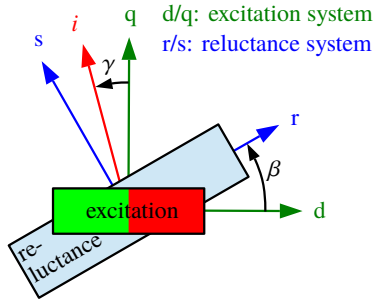
Fig. 1: Basic reference frames of machines with a displaced reluctance axis according to [6].
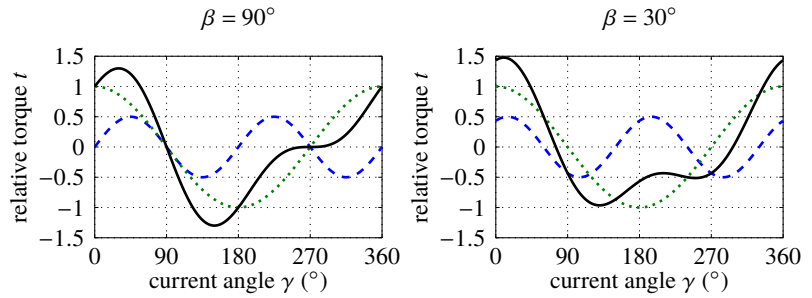
Fig. 2: Reluctance torque (blue, dashed), synchronous torque (green, dotted) and total torque (black, solid) of a PMSM with $\beta = 90°$ (left) or $\beta = 30°$ (right) for constant current magnitude.

machine with a displaced reluctance axis (HSM/DRA), which exhibits the same benefits as mentioned before, yet its main feature is the improved performance due to the magnetic asymmetry. On the downside, this asymmetry causes lower performance in generating mode.

This contribution proposes an advanced version of the HSM/DRA, whose geometry is designed to yield identical performance in motoring and generating mode. This is accomplished by a design which is capable of inverting the magnetic asymmetry dynamically while in operation. To confirm the benefits of this geometry, a prototype has been designed, simulated, built and tested. As a reference, a conventional EESM prototype of the same size and rating has been built as well.

The theoretical background and the working principle of the proposed geometry are discussed in the following Section as well as the prototype motors and the test bench. After that, measurement results concerning the fundamental wave behavior of the machines are given. The subsequent Section examines harmonic effects which influence torque and additional losses. Finally, the overall efficiency of the motors is given and the benefits of the proposed geometry are shown.

Theoretical Background

The basic idea behind synchronous machines with a displaced reluctance axis has been developed in [6]. Their concept is the spatial displacement of the two torque producing principles in synchronous machines – the synchronous torque, which is produced by the rotor excitation, and the reluctance torque, which is produced by the saliency of the rotor lamination.

Fig. 1 shows a simplified drawing of the rotor of a generalized PMSM, which consists of two independent parts. The red and green part represents the rotor excitation, the blue part illustrates the simplified salient rotor structure. As usual for conventional machines, the d/q reference frame is aligned to the direction of the rotor excitation, which is also used to define the angle γ of the stator current space vector i. The r/s reference frame is aligned to the direction of the lowest magnetic reluctance, i.e. the greatest inductance. In the example of Fig. 1, the geometry yields a displacement angle β of 30°.

Conventional PMSMs with interior magnets typically yield $L_d < L_q$ [1], which is equivalent to $\beta = 90°$. The left diagram in Fig. 2 shows the torque curve of this kind of machines when the stator current magnitude abs(i) is held constant but the angle γ of the current space vector is varied. The angle which leads to the maximum synchronous torque ($\gamma = 0°$) is not equal to the angle which leads to maximum reluctance torque ($\gamma = 45°$). Therefore, the maximum of the resulting torque lies between these two angles, which means that both torque producing principles are not utilized entirely. Due to the symmetry of the rotor structure, the maximum absolute torque in motoring and generating mode are equal.

The right diagram in Fig. 2 shows the torque curves for a machine with $\beta = 30°$, whose simplified structure is given in Fig. 1. The amplitude of each single torque component is the same as in the left diagram. Obviously, maximum motoring torque is greater in this case as the maxima of the two torque producing principles are closer together. However, torque capability in generating mode is inferior as the two effects generate torque in opposite directions.
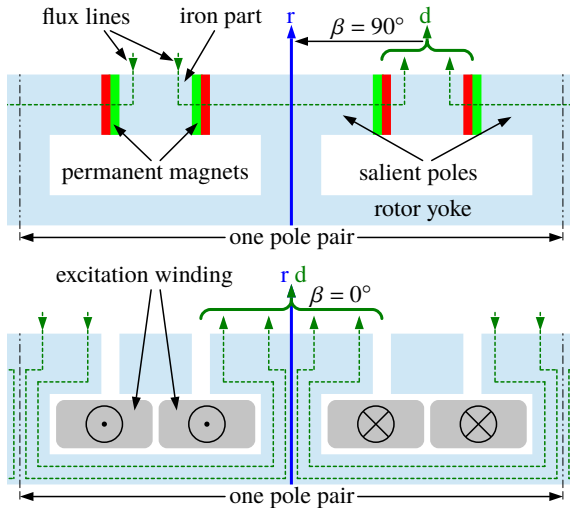
Fig. 3: Simplified structure of two poles of the rotor with only PMs active (top) resp. only electric excitation active (bottom).
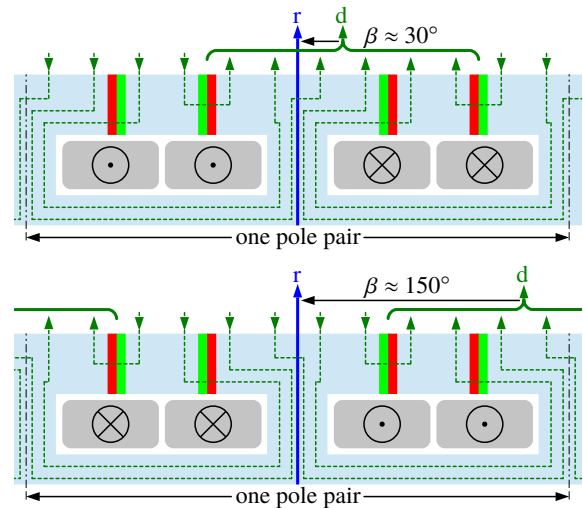
Fig. 4: Simplified structure of two poles of the rotor with positive (top) and negative (bottom) excitation current (PMs active).

Proposed Rotor Geometry

While theoretical studies about the optimum displacement angle β regarding inverter utilization have been carried out in [6], a more practical approach concerning the feasibility of such machines has been made in [5]. It was proven that hybrid machines using both PM and electric excitation are most suitable for machine designs with a displaced reluctance axis. However, the proposed HSM/DRA geometry suffers from the disadvantage of inferior generating performance as described above.

Working Principle

To avoid this effect, a machine design is proposed which is capable of inverting the displacement angle β while in operation, thereby swapping motoring and generating performance. Fig. 3 and Fig. 4 are given to clarify the working principle. The geometry basically consists of a salient pole structure with excitation windings and PM parts. Each PM part consists of two PMs which enclose an iron part.

Fig. 3 (top) shows the magnetic condition if only the PMs are active: North and south poles are created on the rotor surface which are displaced by $\beta = 90°$ from the r axis. If only the excitation winding is considered (PM removed for clarity), the r axis and the d axis coincide (lower diagram, $\beta = 0°$).

The superposition of both cases (active PMs and excitation winding) is depicted in Fig. 4 (top): The north and south poles on the rotor surface originating from the PMs and the excitation winding create common poles, whose centers are displaced from the r axis by $0° < \beta < 90°$, where $\beta \approx 30°$ is a usual value.

It is worth noticing that one PM of a PM part draws the flux lines from the adjacent salient pole while the other PM attracts flux lines which already crossed the rotor yoke. This means that a part of the air gap flux does not pass the rotor yoke which leads to lower rotor saturation as opposed to conventional EESM designs. This can be used to design the salient poles narrower to gain space for the PM parts and to reduce rotor saturation.

The magnetic condition on the surface and on the inside of the rotor is entirely mirrored if the sign of the excitation current is altered. This situation is depicted in Fig. 4 (bottom). While the PM poles remain in the same place, the polarity of the electrically excited poles is inverted. The resulting poles on the rotor surface are shifted along the rotor perimeter in a way that the value of β grows greater than $90°$. Regarding the values of β and the excitation current, the axis at $\beta = 90°$ acts as a symmetry axis if the sign of the excitation current is altered.
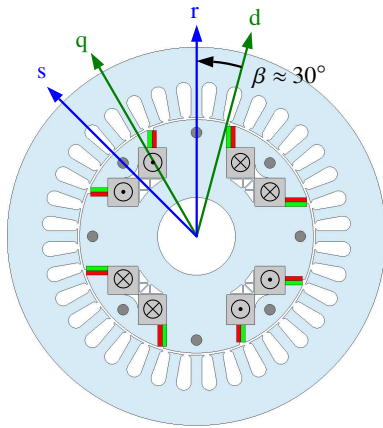
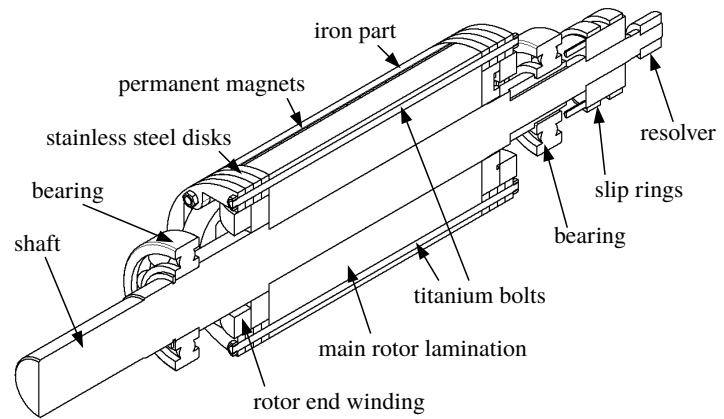Fig. 5: Cross section of the proposed HSM/DRA geometry.

Fig. 6: Longitudinal section of the proposed HSM/DRA rotor geometry. This drawing is the basis of the prototype (see Fig. 8).

Design Considerations

Fig. 5 shows the cross section of the proposed machine. The longitudinal section is depicted in Fig. 6. To deal with real-world concerns, three major issues have been addressed in the prototype:

- The PM and iron parts between the salient poles are subject to centripetal forces because they are not inherently joint to the main rotor part. The proposed geometry uses axial bolts made of titanium, which are embedded in the iron parts and the salient poles (grey circles in Fig. 5). On both sides, they are mounted to stainless steel disks. Thus, the iron pieces are held by the disks, which are in turn held by the main rotor part. The PM are retained in their position by small noses on the salient poles. For further stability, the rotor is resin-impregnated.

- As the PMs and the iron parts cover the axial coil sides of the rotor winding entirely, cooling is more difficult. Therefore, cooling channels are integrated in the main rotor part on the inside surface of the winding area. A fan mounted on the bearing shield forces an airflow through the cooling channels and the air gap.

- The basic structure of Fig. 4 introduces a large amount of air gap harmonics, as the air gap width is held constant to achieve maximum air gap flux density, leading to severe torque ripple and other effects (see Section "Harmonic Behavior"). Instead of rotor skewing, which makes assembly difficult and expensive, the individual position of the PM has been altered between adjacent poles. Their positions vary in the range of one stator tooth pitch, which reduces torque ripple significantly.

Prototypes

In order to prove the benefits of the proposed geometry, an HSM/DRA and a conventional EESM prototype have been designed using finite element analysis (FEA) and numerical optimization. Both rotors have been optimized regarding torque, efficiency and torque ripple.

To maintain comparability, the same stator type has been used and the electric values of the rotors (turn number, wire cross section, slip rings) are equal. The stators originate from identical standard industry induction motors of frame size 132 with 2 pole pairs. The stator winding is symmetric and star-connected with the star point not connected to the inverter. Stators and rotors are not skewed.

The common machine data can be found in Table I and in Table II. Photographs of the prototype rotors are given in Fig. 7 and Fig. 8.

To reduce the risk of mechanical destruction of the prototypes, the maximum speed is limited to $n_\mathrm{max} = 3000\,\mathrm{min}^{-1}$. However, to achieve a wide field weakening range, the stator voltage limit is reduced from 400 V of the original induction machine to 240 V.

Fig. 7: EESM prototype rotor.

Fig. 8: HSM/DRA prototype rotor.

Table I: Common Nominal Electrical Machine Data

	stator values	rotor values
line voltage	240 V	48 V
line current	10.1 A	13 A
phase resistance (20°C)	0.94 Ω	1.26 Ω

Table II: Mechanical Data

	dimensions
stator diameter	175 mm
bore diameter	110 mm
active length	160 mm

Test Bench

Both prototypes are mounted back-to-back on a test bench for detailed examination of each motor. Depending on the type of measurement, one of the motors acts as speed controlled load machine while the other motor is the device under test. A photograph of the test bench is given in Fig. 9.

The test bench is powered by an in-house inverter and measurement system [7]. It consists of two digital signal processor (DSP) systems based on the TMS320C6748 by Texas Instruments, two modulators based on a field programmable gate array of the Cyclone series by Altera and IGBT inverters of the type FS75R12KT4 by Infineon. Torque is measured using the torquemeter DRFL-III by ETH Messtechnik, rotor speed and position are detected by two resolvers of the type RE-15-1-A15 by LTN Servotechnik.

The inverter is operated at a switching frequency of 8 kHz. All calculations of the control algorithms are executed within the corresponding time interval. Both machines are current controlled using model predictive control algorithms based on the direct flux linkage connection method presented in [8]. The necessary flux linkage functions are derived from preceding FEA calculations and are stored as look-up tables on the DSP system.
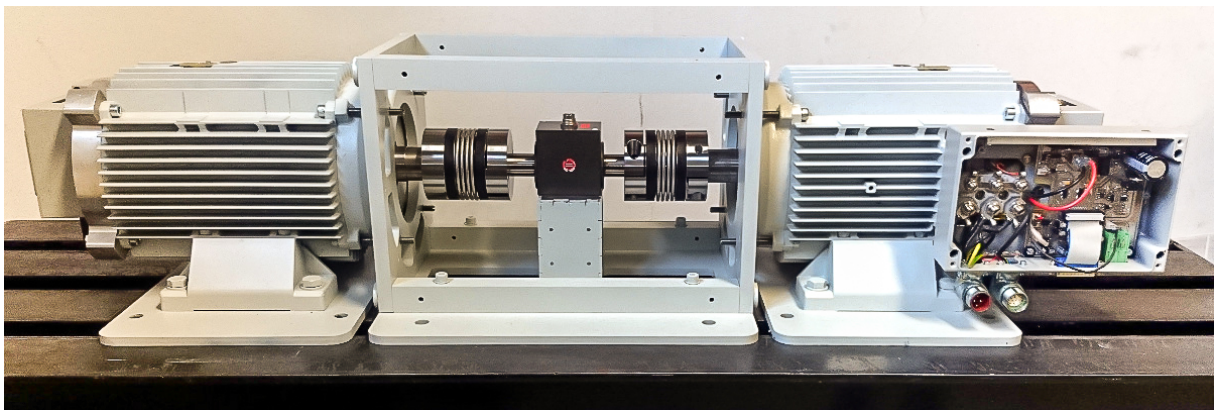

Fig. 9: Both prototypes are mounted back-to-back via a torquemeter on a test bench. The full bridge inverter for the rotor circuit is integrated in the terminal box. Additional housing fans are not shown.

Stationary Behavior

The machines discussed in this paper differ from PMSMs only in the rotor. The stator voltage equations can therefore be adopted from [8], where the indices d and q are replaced by r and s:

$$v_r = R_S i_r + \frac{d\psi_r}{dt} - \omega\psi_s \qquad v_s = R_S i_s + \frac{d\psi_s}{dt} + \omega\psi_r \qquad v_S = \sqrt{v_r^2 + v_s^2} \qquad (1)$$

R_S denotes the stator resistance, t the time, ω the electric angular frequency and v_x, i_x, ψ_x the voltage, current and flux linkage components of the r axis ($x = r$) and the quadrature axis ($x = s$). Using the r/s-system has considerable practical benefits such as the direct evaluation of the resolver signals.

The voltage equation of the field winding (f) of the rotor is expressed as:

$$v_f = R_f i_f + \frac{d\psi_f}{dt} \qquad (2)$$

Using this set of equations, the stationary behavior of the machines can be measured and described. To keep the equations simple, the dependency of machine parameters on other quantities is omitted in the equations but considered in the measurement results. It must be kept in mind that R_S and R_f are temperature dependent and ψ_x with $x \in \{r, s, f\}$ are dependent on all three current components and on the rotor angle. However, the latter dependency is neglected by averaging.

Flux Linkage Measurements

The measurement routine of the flux linkages is strongly oriented on [9]. It establishes all the desired current sampling points sequentially while maintaining a certain machine temperature. At each current sampling point, v_r and v_s are measured. Using these voltages and the fact that the operation points are stationary (i.e. $d/dt = 0$), the desired values of ψ_r and ψ_s are calculated using Eq. (1).

Eq. (2) clarifies that this approach is unsuitable to determine the value of ψ_f as there is only a time dependent summand in this equation. Therefore, the dynamic voltage trajectories have to be evaluated when the current sampling point (i_r^*, i_s^*, i_f^*) is established:

$$\psi_f(i_r^*, i_s^*, i_f^*) = \int_{t_0}^{t_1} v_f(t) - R_f i_f(t) \, dt + \psi_f(t_0)$$

with $i_r(t_0) = i_s(t_0) = i_f(t_0) = 0$ and $i_r(t_1) = i_r^*, i_s(t_1) = i_r^*, i_s(t_1) = i_f^*$ 　　　(3)

There, $\psi_f(t_0)$ is always zero as there is no rotor flux in the r axis when the currents are zero because the PM flux is perpendicular to the r axis. An example operation point is shown in Fig. 10. The integration of $v_f - R i_f$ starts at $t = 0\,$s when the rotor voltage first hits its limit.
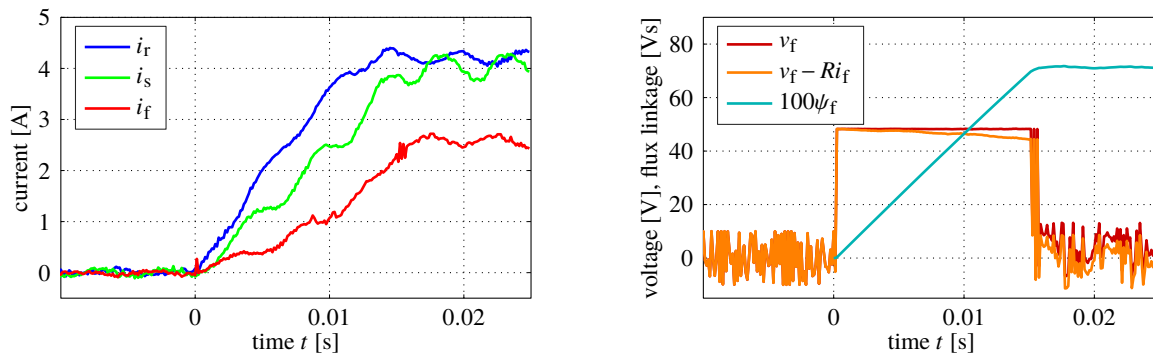

Fig. 10: Evaluation of the step response to find the value of ψ_f: currents (left), voltages and flux linkage (right). The ripples due to machine harmonics have to be treated in post processing.
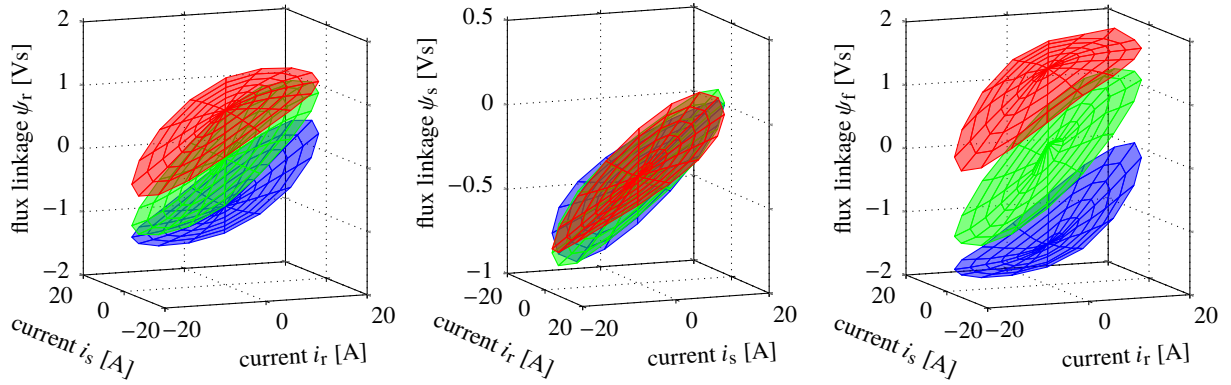
Fig. 11: Measured flux linkages ψ_r (left), ψ_s (middle), ψ_f (right) at $i_f = -13\,\text{A}$ (blue), $i_f = 0\,\text{A}$ (green) and $i_f = +13\,\text{A}$ (red).

Fig. 11 shows the measured flux linkages in the three axes r, s and f in dependency on the stator current for different rotor currents of the HSM/DRA. The flux variation in the r axis is stronger because the magnetic resistance is lower due to the rotor iron core. The PMs in the s axis increase the magnetic resistance. Further, saturation effects in the d and f axis are evident as the curves show variable gradients in both directions. The s axis shows lower saturation effects as the PMs increase the effective air gap. The slope of ψ_f is very similar to that of ψ_r as both axes are strongly coupled. The difference in absolute values originates from the d and f axis winding factors.

The offset at $i_r = i_s = 0\,\text{A}$ of the ψ_r plot is caused by the rotor field winding flux and is dependent on i_f. The offset of the ψ_s plot originates from the PMs and is almost constant. Both of them define the excitation current dependent displacement angle β:

$$\beta(i_f) = \arctan \frac{-\psi_s(i_r = 0\,\text{A}, i_s = 0\,\text{A}, i_f)}{\psi_r(i_r = 0\,\text{A}, i_s = 0\,\text{A}, i_f)} \tag{4}$$

Due to the nonlinear magnetics, this angle is only defined at zero stator current. This equation yields $\beta(i_f = 0\,\text{A}) = 90°$ and $\beta(i_f = 13\,\text{A}) \approx 30°$. This means, at zero excitation current, the machine can be regarded as an IPM with $L_q > L_d$. With increasing excitation current, the asymmetric nature appears and β decreases into the beneficial range of values [5, 6]. The same is true if the excitation current falls below $0\,\text{A}$, then β increases to approximately $150°$, which is beneficial for producing negative torque.

Current Plane

The machine characteristics can be conveniently represented in the current plane [6] using the voltage equations (1) and the measured shaft torque T_{sh}. Fig. 12 opposes the current plane diagrams of the EESM (left) and the HSM/DRA for positive ($i_f = +13\,\text{A}$, middle) and negative ($i_f = -13\,\text{A}$, right) excitation current at shaft speed $n = 1000\,\text{min}^{-1}$. There, the countour lines of the stator voltage v_S are plotted red and the contour lines of the measured shaft torque T_{sh} are plotted blue.

The diagram of the EESM is almost symmetrical to the i_r axis as this machine is magnetically symmetric. Minor deviations arise from measurement uncertainties and the stator resistance, which is visible in the stator voltage.

At $i_f = +13\,\text{A}$, the HSM/DRA (middle diagram) shows the expected asymmetric diagram [5, 6]. The center of the voltage ellipses is not located on any axis and the maximum possible torque without exceeding the current limit is much greater than the absolute value of the minimum possible torque. Compared to the EESM, the maximum torque is slightly greater.

The situation is reversed when the excitation current is inverted (right diagram). In this case, not only the center of the ellipses has moved, but also the maximum absolute generating torque has risen to a value equal to the motoring torque of the former case. This shows that the machine is capable of fully
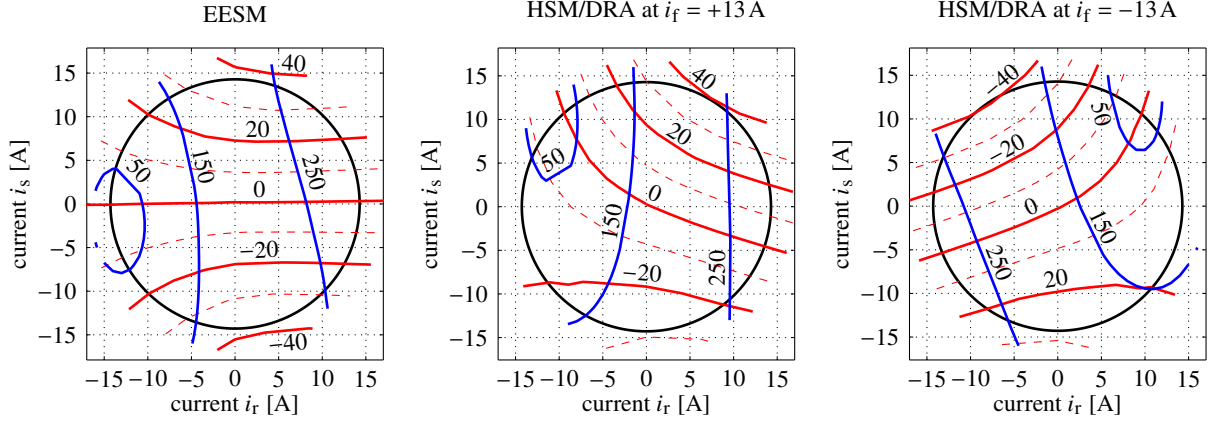
Fig. 12: Current planes of the EESM (left) and the HSM/DRA at $i_f = +13\,\text{A}$ (middle) and the HSM/DRA at $i_f = -13\,\text{A}$ (right). The diagrams show the rated current circle (black), contour lines of the stator voltage v_S [V] at $n = 1000\,\text{min}^{-1}$ (blue) and contour lines of the measured shaft torque T_{sh} [Nm] (red).

symmetric four quadrant operation because it avoids the lower absolute generating torque, a phenomenon that is common to machines with a fixed or limited range of displacement angles [5, 6].

Torque Versus No Load Flux Linkage

Using a representation which compares the torque and the corresponding no load stator flux linkage, it can be shown that the beneficial effects of the displaced reluctance axis are not a result of the additional rotor flux generated by the PMs per se. They are merely used to be able to displace the reluctance axis in the first place.

The diagrams in Fig. 13 compare the inner torque T_i and the no load (i.e. $i_r = i_s = 0\,\text{A}$) flux linkage $\psi_{S,0}$ (Fig. 11) to the necessary excitation current (left, middle) and to each other (right). The inner torque T_i is calculated by

$$T_i = \frac{3}{2}p \cdot \left(\psi_d i_q - \psi_q i_d\right) \tag{5}$$

with the number of pole pairs p. The absolute value of the stator current is kept at its rated value while the current angle has been varied in order to obtain the maximum possible torque (MTPA).

Regarding the left diagram, the offset in $\psi_{S,0}$ at $i_f = 0\,\text{A}$ of the HSM/DRA shows the presence of the PMs. Increasing current leads to a very linear increase in rotor flux linkage of the EESM with slight saturation effects at greater currents. The rotor flux linkage of the HSM/DRA starts to increase at a slow rate initially as the excitation winding becomes effective in the r axis, whereas the PMs are located in the s axis. The slope at greater excitation currents is still not as steep as the slope of the EESM because the salient pole surface at the air gap of the HSM/DRA is narrower (see Fig. 7 and Fig. 8).
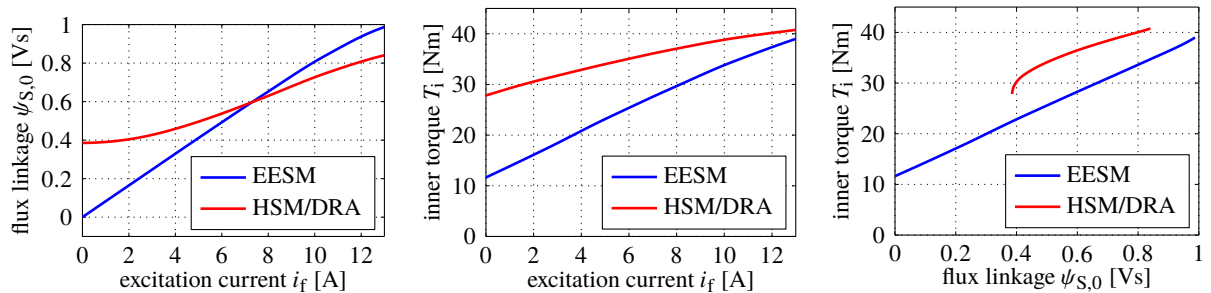

Fig. 13: Dependancies of the excitation current i_f, the no load stator flux linkage $\psi_{S,0}$ and the inner torque T_i of both machines.

Comparing the left and the middle diagram, it is evident that the sole presence of PMs is not the only reason of the torque benefits of the HSM/DRA. At rated excitation current (i.e. $i_\mathrm{f} = 13\,\mathrm{A}$), the no load flux linkage of the HSM/DRA is even smaller than that of the EESM while the torque is greater.

However, the torque of the HSM/DRA rises less steep than the torque of the EESM. This leads to a point at $i_\mathrm{f} \approx 17\,\mathrm{A}$ where the torque of the EESM becomes greater than that of the HSM/DRA (not shown in the diagram). This effect however originates from the much greater no load flux linkage of the EESM at high values of i_f. This distortive effect can be avoided when comparing the torque to the no load flux linkage (right diagram). It is evident that the HSM/DRA is capable of producing greater torque than the EESM at every occurring no load flux linkage, which proves the benefits of the machine concept. However, it must be noted that generating great values of rotor flux requires disproportionately high values of excitation current which makes the HSM/DRA less suitable for efficient high utilization drives.

Harmonic Behavior

As shown in the preceding Section, the rotor flux of the HSM/DRA is significantly lower than that of the EESM, which reduces the maximum achievable torque. It is therefore of high priority to increase the rotor flux as much as possible in the design phase. As can be seen in Fig. 5, this is done by using a uniform air gap, whereas the EESM has rounded pole edges (see Fig. 7). This leads to a heavily distorted rotor field. The effects of this characteristic become evident in multiple physical domains and are investigated in this Section.

Fig. 14 (left) shows the no load air gap flux distribution of the EESM (red) at $i_\mathrm{f} = 13\,\mathrm{A}$ and of the HSM/DRA (blue) at $i_\mathrm{f} = 13\,\mathrm{A}$ which are derived from FEA. While the air gap flux distribution of the EESM resembles the ideal sinusoidal shape in some degree, the distribution of the HSM/DRA shows multiple unfavorable characteristics. Due to the uniform air gap, the transitions in the field distribution are quite steep, thereby producing many higher order harmonics. Also, due to the different flux densities of the PMs and the excitation winding and due to the alteration of the PM position (see Section "Design Considerations"), many odd harmonics are produced. Total harmonic distortion (THD) of the EESM air gap field is $5.31\,\%$ while the HSM/DRA yields $30.60\,\%$.

First, this becomes noticeable in the induced line voltage, which is measured across two stator winding terminals at $n = 468.75\,\mathrm{min}^{-1}$, see Fig. 14 (right). This speed yields exactly 512 measurement points per electrical period. The HSM/DRA shows harmonics of higher frequency. The THD of the induced line voltage is $0.18\,\%$ (EESM) resp. $0.33\,\%$ (HSM/DRA).

A second effect is the increase of torque ripple in different load points. Fig. 15 (left) shows FEA results the torque ripple of both machines in their rated operation point. To rule out the influence of the other machine, this investigation can not be executed on the test bench. The EESM yields a peak-to-peak value of $3.14\,\mathrm{Nm}$ ($8.09\,\%$) whereas the HSM/DRA yields $5.97\,\mathrm{Nm}$ ($14.2\,\%$).

The spatial harmonics of the air gap field cause iron losses which increase with rising amplitudes of the harmonics. To investigate this effect on the test bench for the prototype machines, the machine set
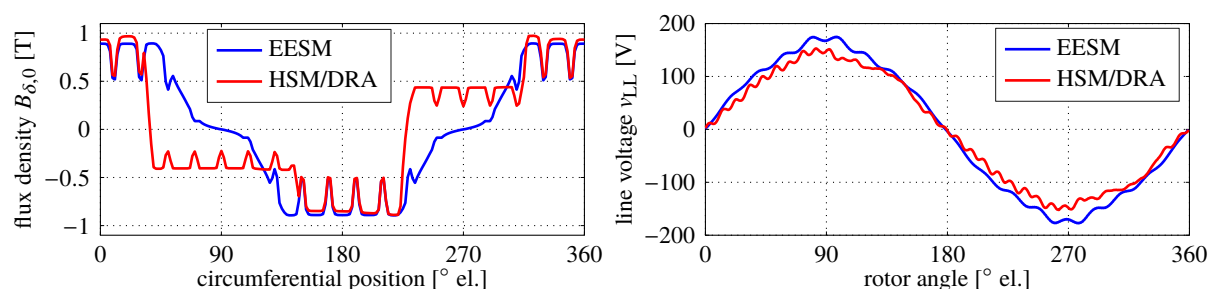

Fig. 14: The HSM/DRA (red) shows a greater harmonics content in the air gap field (left, FEA) which yields greater harmonics content in the no load line voltage (right, measurement). $i_\mathrm{e} = +13\,\mathrm{A}$ in all cases.
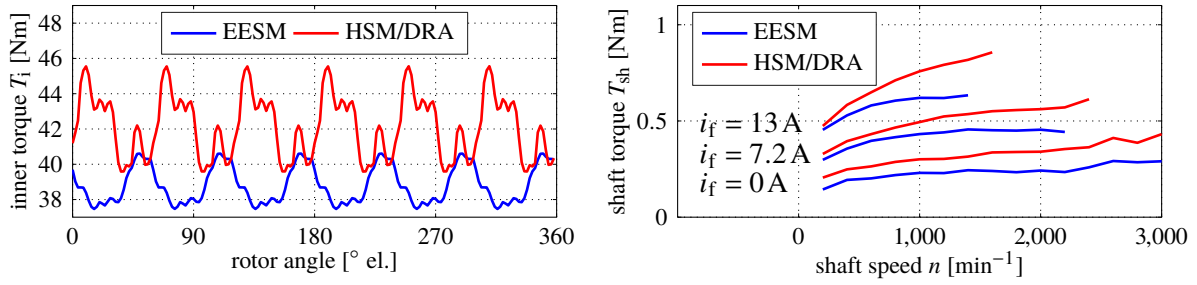
Fig. 15: The HSM/DRA (red) also shows a greater torque ripple (left, FEA, rated operation point shown) and a greater no load braking torque (right, measurement).

was accelerated to various speeds using one machine while various excitation current values at zero stator current were impressed on the second machine. This test was carried out with both machines and both directions of rotation to rule out offset errors. The resulting shaft torque was measured, which represents the braking torque generated by windage and friction losses as well as iron losses. Fig. 15 (right) shows the results of both machines for speeds in the range of $200\,\mathrm{min}^{-1} \leq n \leq 3000\,\mathrm{min}^{-1}$ and $i_\mathrm{f} \in \{0\,\mathrm{A}, +7.2\,\mathrm{A}, +13\,\mathrm{A}\}$. The HSM/DRA yields 10 to 40 % greater losses, which can be blamed to iron losses caused by air gap field harmonics, assuming equal windage and friction losses of both machines. However, this is only up to 44 W of power loss and is overcompensated by the intrinsic machine benefits.

Efficiency

Using the measured flux linkage data (see Fig. 11) and the resistance values of both machines, optimum current values regarding overall copper losses were calculated for a fine set of speeds and shaft torques while meeting current and voltage boundaries.

All of these load points were established on the test bench and machine currents $i_\mathrm{r}, i_\mathrm{s}, i_\mathrm{f}$, machine voltages $v_\mathrm{r}, v_\mathrm{s}, v_\mathrm{f}$, the shaft speed n, the shaft torque T_sh and the stator end winding temperature ϑ_S were recorded. The machine under test was preheated to a rotor temperature of 60°C which was kept within a range of ± 2°C during the measurement by introducing heating and cooling phases [9]. The rotor temperature was estimated by evaluation of the no load stator voltage using a reference voltage at 20°C and the data sheet values of the temperature coefficient of the PMs. In the case of the EESM, the stator end winding temperature was controlled. All ohmic losses have been recalculated for 60°C using the actual temperature at the load point. The differences in efficiency between motoring and generating mode derive from measurement uncertainties of the direct measurement method.
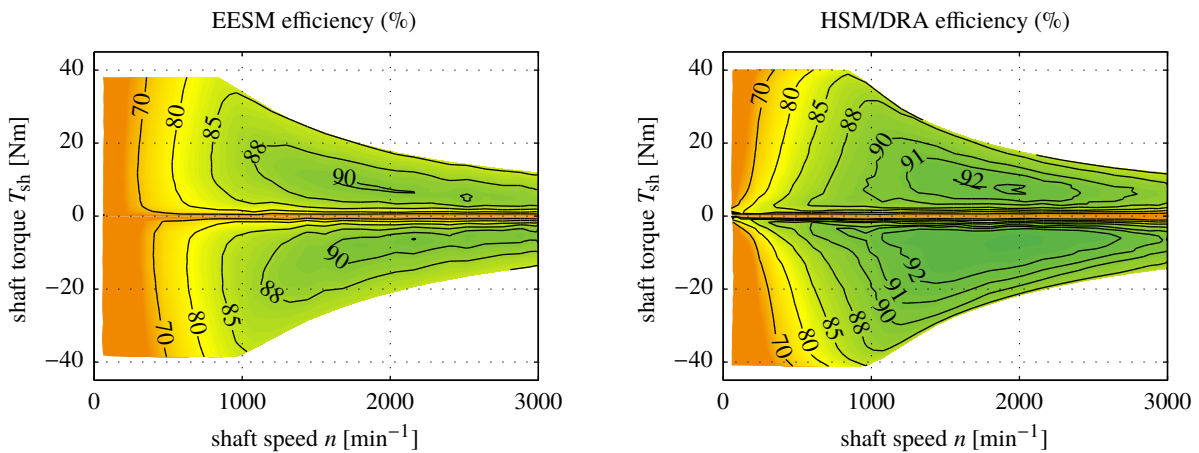

Fig. 16: Measured efficiency maps of the EESM (left) and the HSM/DRA (right). The HSM/DRA delivers greater peak and average efficiency as well as greater maximum torque.

Fig. 16 shows the efficiency maps of the HSM/DRA and the EESM, which are calculated from the measured values using

$$\eta(T_{\mathrm{sh}} \geq 0) = \frac{T_{\mathrm{sh}} \cdot \frac{\omega}{p}}{\frac{3}{2} \cdot (u_{\mathrm{r}} \cdot i_{\mathrm{r}} + u_{\mathrm{s}} \cdot i_{\mathrm{s}}) + u_{\mathrm{f}} \cdot i_{\mathrm{f}}} \qquad \eta(T_{\mathrm{sh}} < 0) = \frac{\frac{3}{2} \cdot (u_{\mathrm{r}} \cdot i_{\mathrm{r}} + u_{\mathrm{s}} \cdot i_{\mathrm{s}}) + u_{\mathrm{f}} \cdot i_{\mathrm{f}}}{T_{\mathrm{sh}} \cdot \frac{\omega}{p}}. \tag{6}$$

Fig. 16 reveals the benefits of the proposed HSM/DRA: First, its maximum torque is increased by 4 % due to the displaced reluctance axis and the fact that the rotor iron is less saturated [5]. Second, its peak efficiency is increased by 2 percentage points and the high efficiency region is notably greater than that of the EESM, especially in the low speed and in the low torque region. Third, compared to the HSM/DRA design of [5], the generating mode is fully usable and shows no efficiency drawbacks.

Conclusion

In this contribution, an HSM/DRA machine geometry is proposed, providing the theoretical benefits of the displaced reluctance axis such as greater torque and efficiency while avoiding its inherent disadvantage of a lower generating torque.

Using test bench measurements and FEA, it is shown that the HSM/DRA yields superior performance over a conventional EESM which is designed using the same base values. Maximum torque, peak efficiency and average efficiency in the torque vs. speed plane are significantly improved.

Several disadvantageous characteristics such as increased spatial harmonics, which lead to increased losses and torque ripple, are identified. However, it is shown that the additional losses are overcompensated by the intrinsic machine benefits.

Because the HSM/DRA has rather low downsizing capabilities, maximum speed limitations due to centripetal forces and a complex and material intensive structure which leads to high production costs, it is predestined for drive applications that focus on high efficiency and four quadrant applications.

References

[1] W. Soong and T. Miller, "Theoretical limitations to the field-weakening performance of the five classes of brushless synchronous AC motor drive," in *Electrical Machines and Drives, 1993. Sixth International Conference on (Conf. Publ. No. 376)*, 1993, pp. 127–132.

[2] N. Bianchi and S. Bolognani, "Parameters and volt-ampere ratings of a field-oriented induction motor drive for flux-weakening applications," in *Electrical Machines and Drives, 1997 Eighth International Conference on (Conf. Publ. No. 444)*, 1997, pp. 46–50.

[3] C. Rossi, D. Casadei, A. Pilati, and M. Marano, "Wound rotor salient pole synchronous machine drive for electric traction," in *Industry Applications Conference, 2006. 41st IAS Annual Meeting. Conference Record of the 2006 IEEE*, vol. 3, 2006, pp. 1235–1241.

[4] Y. Amara, L. Vido, M. Gabsi, E. Hoang, A. Hamid Ben Ahmed, and M. Lecrivain, "Hybrid excitation synchronous machines: Energy-efficient solution for vehicles propulsion," *Vehicular Technology, IEEE Transactions on*, vol. 58, no. 5, pp. 2137–2149, 2009.

[5] P. Winzer and M. Doppelbauer, "Comparison of synchronous machine designs with displaced reluctance axis considering losses and iron saturation," in *Electric Machines & Drives Conference (IEMDC), 2015 IEEE International*, 2015, pp. 1801–1807.

[6] P. Winzer and M. Doppelbauer, "Theoretical analysis of synchronous machines with displaced reluctance axis," in *Electrical Machines (ICEM), 2014 International Conference on*, 2014, pp. 641–647.

[7] C. Axtmann and M. Boxriker and M. Braun, "A Custom, High-Performance Real Time Measurement and Control System for Arbitrary Power Electronic Systems in Academic Research and Education," in *Power Electronics and Applications (EPE'16-ECCE Europe), 2016 18th European Conference on*, Karlsruhe, 2016, accepted for publication

[8] J. Richter and M. Doppelbauer, "Predictive trajectory control of permanent magnet synchronous machines with nonlinear magnetics," *IEEE Transactions on Industrial Electronics*, 2016, accepted for publication, DOI 10.1109/TIE.2016.2527628.

[9] J. Richter, A. Dollinger, and M. Doppelbauer, "Iron loss and parameter measurement of permanent magnet synchronous machines," in *Electrical Machines (ICEM), 2014 International Conference on*, 2014, pp. 1635–1641.